International Journal of Solids and Structures 49 (2012) 1900–1907

Contents lists available at SciVerse ScienceDirect

International Journal of Solids and Structures

journal homepage: www.elsevier.com/locate/ijsolstr

Crack growth in planar elastic fiber materials

P. Isaksson [a,*], P.J.J. Dumont [b], S. Rolland du Roscoat [c,d]

[a] Applied Mechanics, The Ångström Laboratory, Uppsala University, Box 534, 751 21 Uppsala, Sweden
[b] Laboratoire de Génie des Procédés Papetiers, CNRS/Grenoble INP, BP 65, 38402 Saint-Martin-d'Hères, France
[c] Laboratoire Sols-Solides-Structures-Risques, CNRS/INP-UJF Grenoble, BP 53, 38041 Grenoble, France
[d] European Synchrotron Radiation Facility, ID 19, 38043 Grenoble, France

ARTICLE INFO

Article history:
Received 16 May 2011
Received in revised form 9 March 2012
Available online 11 April 2012

Keywords:
Fiber network
Crack mechanics
Nonlocal theory
Synchrotron microtomography
In situ mechanical test

ABSTRACT

Particularly attention is here given to crack growth in opening mode in fiber networks. Low- and high-density cellulose fiber materials are used in synchrotron X-ray microtomography tensile experiments to illustrate phenomena arising during crack growth. To capture the observed fundamental mechanisms, significantly different from classical continua, a mechanical model based on a strong nonlocal theory is applied in which an intrinsic length reflects a characteristic length of the microstructure. Nonlocal stress and strain tensor fields are estimated by analytical solutions on closed form to a modified inhomogeneous Helmholtz equation using LEFM crack-tip fields as source terms. Justified by experimental observations, physical requirements of finite stresses and strains at infinity and at the tip are applied to remove singularities. The near-tip nonlocal hoop stress field is used to estimate crack growth directions and sizes of fracture process zones. Experimental observations are shown to be qualitatively well in accordance with numerical predictions, which justifies the adopted approach.

1. Introduction

Living tissues such as bones, muscles and plant stems are examples of natural fiber networks. Manufactured fiber materials are commonly encountered in the automotive and aerospace industry and are used, e.g., for filtration processes or medical applications. Traditional paper mainly consists of cellulose fibers, which are about thousand times larger than fibers in recently developed cellulose nanofibril networks (Henriksson et al., 2008). Common textiles are made of cotton and polyester fibers. Several biomedical implants are currently being developed to mimic the human tissue behavior. Modern non-woven felts are made of, e.g., nanofibers (Dzenis, 2004) or non-woven glass-fibers (Ridruejo et al., 2010, 2011). Although these materials may, at a first look, appear different they are in fact very similar from a structural point of view: fiber network materials are all composed of structural fibers connected at intersections by bonds.

The evolution of microscopic fracture, which precedes macroscopic crack growth and ultimate failure, in such materials is a very complex process that depends strongly on, among other things; the volume fraction of fibers and pores, the microstructure and the mechanical properties of material constituents. The microscopic fractures are observed as diffuse material damage on the macroscopic scale. Due to its complex nature, the understanding of fracture processes in fiber network structures is still in its infancy.

Traditionally, hypotheses for calculation of crack paths may be divided into those based on propagation and those based on projection. Propagation criteria study the crack-tip state of a hypothetical extension of the crack whereas projection based criteria study the mechanical state ahead of the crack-tip. For linear elastic crack growth, an assumption of a kink in a direction giving a pure opening mode is frequently used. An example of a projective criterion is to assume that the crack grows in the plane were the largest hoop stress acts. The variety of hypotheses has been extensively discussed in the past, cf. (Kalthoff, 1973; Erdogan and Sih, 1963; Cotterell and Rice, 1980). However, Bergqvist and Guex (1979) reported that the direction of crack growth for small deviations from the path straight ahead to a large extent is independent of the choice among the most generally used criteria as long as the material can be treated as a homogeneous elastic continuum. These fracture theories have formed the basis for the fracture analyses that are performed today in, e.g., the paper industry. However, it is known, cf. (Hägglund and Isaksson, 2006), that sparse network structures (e.g. tissue papers) are not as sensitive to defects as dense paper materials (e.g. newsprint). In a sparse network, a relatively large defect size is required to localize macroscopic fracture: a behavior that is in contradiction with the classical fracture theories. So, why are sparse network structures relatively insensitive to flaws? Is there a convenient way to handle this

* Corresponding author.
E-mail address: per.isaksson@angstrom.uu.se (P. Isaksson).

0020-7683/$ - see front matter © 2012 Elsevier Ltd. All rights reserved.
http://dx.doi.org/10.1016/j.ijsolstr.2012.03.037

phenomenon on the macroscopic scale? These are questions the present study aims to answer.

The classical fracture theories are all described by traditional continuum theories, which rely heavily on the inherent assumption that material properties vary continuously throughout the body. However, certain heterogeneities linked to the microstructure of the fiber network cannot be readily described within such framework. This is due to a size-effect in the mechanical behavior of the network occurring when a high-strain gradient is present. The fibers introduce long-range microstructural effects in the material that distribute macroscopic stresses and strains in a complex manner (Isaksson and Hägglund, 2009a,b). If a macroscopic crack is present, fibers distribute stresses near the crack-tip and thus reduce the probability of failure immediately ahead of the crack since forces are transferred to remote regions from the tip. This structural phenomenon is pretty much resembled in the classical game "Mikado". Nonlocal theories provide a framework that enables microstructural effects to be included in a continuum theory by introducing an internal length scale in the governing equations that relates to the dimensions of the microstructure and material constituents. The difference between a local and nonlocal model may become apparent when inspecting Fig. 1.

A number of nonlocal theories have been presented in the last decades (cf. Fleck and Hutchinson, 1993, 1997; Fleck et al., 1994; Gao et al., 1999; Huang et al., 2000; Mentzel and Steinmann, 2000; Peerlings et al., 2001; Simone et al., 2004). The various theories are fairly different with respect to the structure of the equations, however, each aims to capture boundary layer phenomena related to phase and grain boundaries, or slips in single crystals, within small deformation formulations. All these theories are considered weakly nonlocal in character because the governing equations in a point include gradients explicitly obtained from state variables in an arbitrary small neighborhood of that point. In the present study, however, a strong nonlocal small deformation theory is used, which is derived by implicitly including gradients on a considerable larger distance. This approach is physically motivated since fibers in, e.g. cellulosic networks, often have the length of millimeters as compared to microns, or even smaller lengths, in the case of dislocation movements in metals.

2. Experimental observation of crack growth in network structures

Both low- and high-density paper materials are examined to illustrate mechanical phenomena taking place during crack propagation in a fiber-based material. The low-density paper was manufactured at very low speed in a so-called through air drying (TAD) process resulting in a sparse network having approximately transversely isotropic mechanical properties. The material was made from bleached unbeaten softwood chemical pulp to a basis weight of 20 g/m^2 and an average thickness of 115 μm. The apparent density of this material is on the average about 174 kg/m^3. The high-density paper is a kraftliner of 140 g/m^2 with a thickness of 158 μm and an apparent density about 886 kg/m^3 manufactured using virgin fibers extracted from a chemical pulp. This material exhibits preferential fiber orientation and thus a mechanical anisotropy, which can be appraised, e.g., by the ratio of its elastic moduli along the machine and cross directions equal to 3.2.

Several rectangular notched specimens were subjected to interrupted tensile tests in situ during microtomography experiments, Fig. 2, i.e. a small displacement (see legends of Figs. 3 and 4) was applied step-by-step to the specimen, which allowed the crack to propagate in a stabile manner and the microtomographs to be taken. The dimensions of the specimens were 6 mm × 2.8 mm. An initial straight crack with a length of 3 mm was cut using a razor blade. Thus, the ratio between initial crack length and the total width of the specimen was always equal to 0.5. Several loading steps were applied using an in-house manufactured tensile machine. As shown on the schematic view of Fig. 2, the specimen is fastened to a fixed lower clamp and an upper clamp, which is vertically actuated by a piezoelectric motor (PiezoMotor Piezo Legs Linear 450 N with a maximum displacement range of 20 mm, Uppsala, Sweden). In the case of dense paper material, the pre-fabricated slit was cut in the machine direction and consequently the loading axis was along the cross direction of the material. It should here be mentioned that specimens were also manufactured with the slit oriented in the perpendicular direction, i.e. along the cross direction. Post analyses of tensile experiments, however, revealed that the orientation of the crack has minor influence on the cracking behavior in the material and for the sake of clarity we are in the following only considering specimens with slits oriented in machine direction (and loaded in cross direction).

The tensile machine was mounted in the microtomograph of the beamline ID19 of the European Synchrotron Radiation Facility (ESRF), Grenoble, France. During the tests, the temperature and the relative humidity of the air surrounding the specimen was about 20°C and 45% RH. All images were acquired using an absorption X-ray microtomography mode. During data acquisition, a parallel and monochromatic X-ray beam (34 keV) irradiated the specimen. Radiographs of the X-ray beam passing through the sample were recorded for 700 different angular positions between 0° and 180°. The exposure time was 0.3 s per radiograph. Notice that the above-mentioned scanning parameters were carefully chosen so as to limit the influence of the irradiation dose on the mechanical properties of the tested specimens. This will be explained in detail

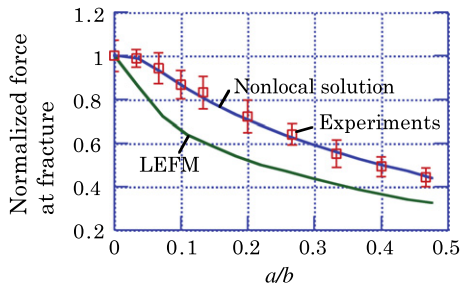

Fig. 1. Fracture loads in tensile tests on a sparse paper from Hägglund and Isaksson (2006). The length a of a slit (located perpendicular to the load direction) is normalized with respect to the specimen's width b and fracture load against the tensile strength of an unnotched material. The local model is given by linear elastic fracture mechanics (LEFM).

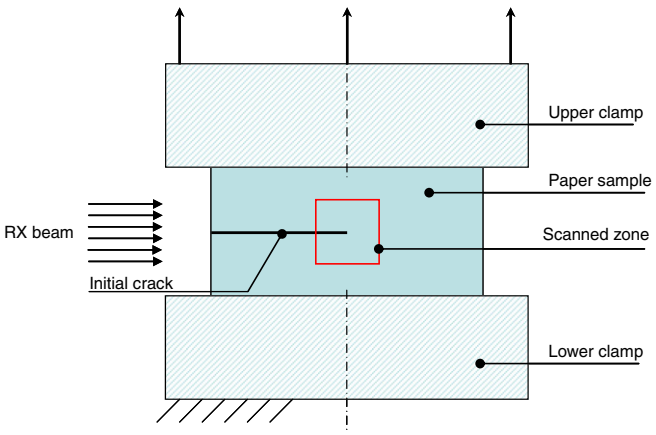

Fig. 2. Schematic view of a paper specimen containing an initial crack.

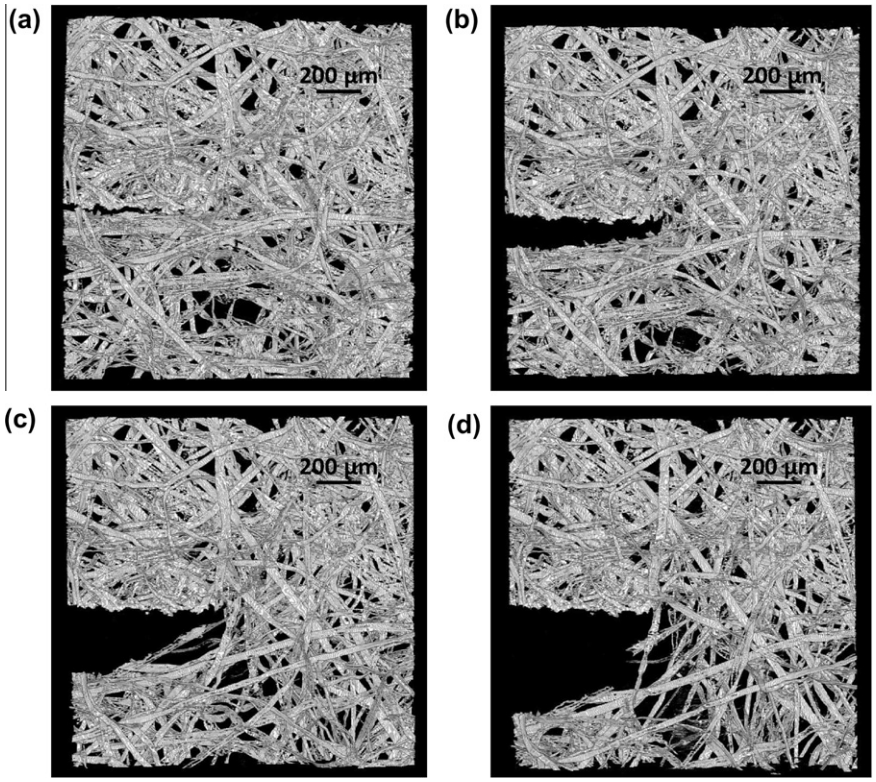

Fig. 3. 3D views of a notched specimen made of a tissue during a tensile experiment. (a) Initial state, (b) crack opening of 150 μm, (c) crack opening of 300 μm and (d) crack opening of 475 μm. The continued crack growth is very diffuse and takes place more or less simultaneously at several places around the main crack via opening of pores. Notice that fibers appear in grey, pores appear in black.

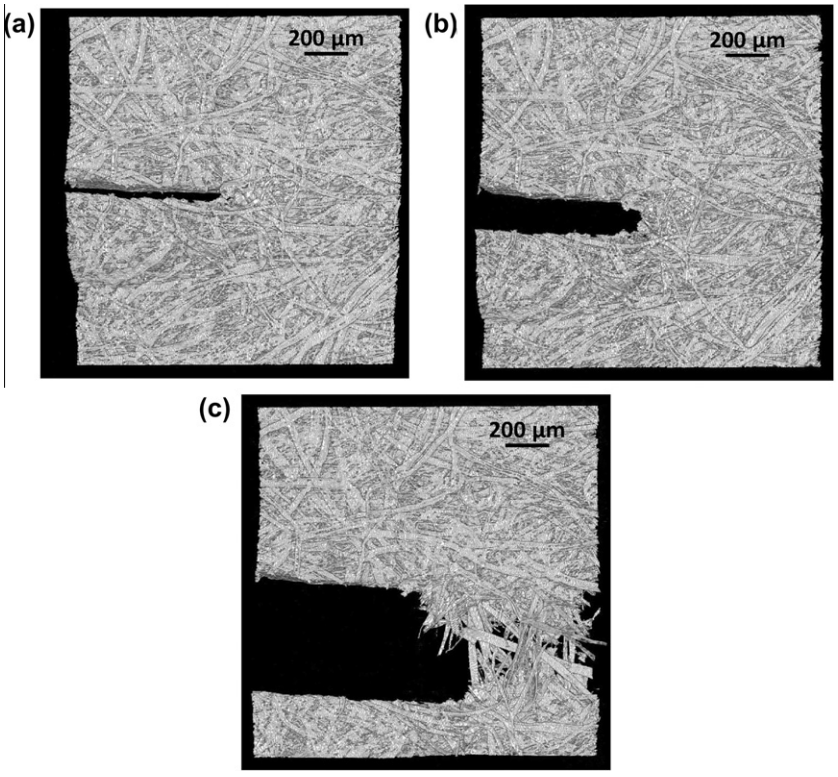

Fig. 4. 3D views of a notched specimen of a liner during a tensile experiment. (a) Initial state, (b) crack opening of 165 μm and (c) crack opening of 480 μm. The initial crack grows via a sharp kink located straight ahead along the plane of the main crack. Notice that fibers appear in grey, pores appear in black.

in a forthcoming article. A filtered back-projection algorithm (Kak and Slaney, 2001; Baruchel et al., 2000) was applied to reconstruct the 3D structure of the specimens using the scanned radiographs. The reconstructed volumes have a size of $1024 \times 1024 \times 1024$

voxels and each voxel a size of $1.4 \times 1.4 \times 1.4\ \mu m^3$, giving an imaged volume of $1433 \times 1433 \times 1433\ \mu m^3$. The size of the scanned zone is limited by a square region, indicated in Fig. 2, and is mainly localized in front of the tip of the initial crack. The reconstructed volume represents a 3D map of the coefficient of X-ray absorption of the specimen constituents. The values of the absorption coefficients are represented as different values of grey level coded in 32 bits. Acquisition artifacts such as ring artifacts were removed using classical image treatment procedures developed at the ESRF. A segmentation procedure was carried out in order to get a 3D representation of the fiber and porous phases of the materials (Rolland du Roscoat et al., 2005, 2007).

Figs. 3 and 4 show images of the low- and high-density materials at various loading steps, which allow for a qualitative description of the continued crack growth. In its initial state, the low-density paper appears clearly (Fig. 3(a)) as a sparse network, which exhibits structural variations: look-through regions (in black), pores, can easily be observed. This type of structural features is obviously natural for low-density materials. On the contrary, the high-density paper exhibits a significantly more homogeneous structure (Fig. 4(a)). The structural differences can be characterized using, for instance, the average number of fiber-to-fiber per fiber bonds, which can be estimated to roughly 15 for the low density paper and about 65 for the high density paper on the basis of a statistical tube model, considering the average fiber volume fraction, the average fiber length, width and thickness and assuming an in-plane isotropic network (Toll, 1993; Le Corre et al., 2005; Viguié et al., 2011). An average fiber length of 2.2 mm and 1.5 mm were estimated for the low-density and high-density papers, respectively. The fiber width and thickness were estimated to 24 μm and 10 μm for both materials. Although they are relatively well in accordance with some experimental measurements (cf. Batchelor et al., 2006; He et al., 2004) for some other paper fiber networks, it should be noticed that these numbers are only estimates. Obviously, it would be relevant to measure these data using directly the scanned images. However, this is considered cumbersome and requires massive image analysis developments considering the geometrical complexity of wood pulp fibers. The average number of fiber-to-fiber bonds per fiber allows for a rough estimation of the segment length between bonds. In the sparse paper, this length is about 125 μm, whereas it is only about 23 μm in the dense paper. These data appear as being visually reasonable when examining Figs. 3 and 4. These lengths might be considered as a lower bound for the characteristic length governing the crack growth phenomena (cf. Hägglund and Isaksson, 2006; Isaksson and Hägglund, 2009b).

Figs. 3 and 4 give several interesting insights on the crack growth phenomena in fiber networks. For both tested materials, the initial cracks are obviously critical defects. This is not surprising having in mind the relative large crack lengths compared to the width of the specimens. During continued loading, the cracks grow by diffuse damage processes in regions at the tips. Furthermore, the highly porous regions of the low-density paper do not themselves create failure localization zones as it might happen if the length of the initial crack would have been smaller, Hägglund and Isaksson (2006) and Fig. 1. Image analysis further reveals that the cracks grow via bond fractures: such progressive damage mechanism is also observed in, for instance, Ridruejo et al. (2011) in a study of a different kind of fiber network. No fiber fractures occurred during these experiments. It can further be observed that the damaged zone is substantially larger and significantly more diffuse in the low-density paper than in the dense. Unfortunately, due to its relatively large size this zone progressively disappeared from the view field during the loading stages for the low-density paper. In the case of the high-density paper, the damage zone is clearly narrower and easily observable at the tip in all load stages. What is also very interesting is that the continued crack growth in the sparse network occurs via an incipient diffuse kink eventually formed in a direction slightly deviated from the initial crack plane (Fig. 3(d)) while in the dense network, the crack growth continues straight ahead along the main crack plane (Fig. 4(c)). When considering these two limited sets of observations (one of each material), it seems that when decreasing the density of the fiber network, crack growth, which occurs through pronounced damage processes, involves larger regions and may follow deviated paths compared to in higher density fiber networks where the continued crack growth is inclined to take place in a small region at the tip.

3. Implicit gradient nonlocal theory

A nonlocal theory (cf. Pijaudier-Cabot and Bazant, 1987; Eringen, 2002) abandons Saint–Venant's principle of local action, i.e. the assumption that the mechanical state in a given point in a material is uniquely determined by the state in that point only as it includes interactions with a neighborhood to that point. Examples of such theories include nonlocal integral formulations (cf. Kröner, 1967; Eringen and Edelen, 1972; Silling, 2000) and gradient theories (cf. Peerlings et al., 2001; Aifantis, 2011). These theories are based on the assumption that a nonlocal counterpart $\bar{\xi}$ in a point (x_1,x_2) of a local state variable ξ over a surrounding two-dimensional infinite domain Ω is given by spatial averaging in a vicinity of the point according to

$$\bar{\xi}(x_1,x_2) = \frac{\int_\Omega \phi(x_1',x_2';x_1,x_2)\,\xi(x_1',x_2')\,\mathrm{d}\Omega}{\int_\Omega \phi(x_1',x_2';x_1,x_2)\,\mathrm{d}\Omega}, \tag{1}$$

where (x_1',x_2') is the position of the infinitesimal area $\mathrm{d}\Omega$. The weight function ϕ is assumed homogenous, isotropic and having a Gaussian distribution:

$$\phi = (2\pi l^2)^{-1}\exp[-\rho^2/(2l^2)], \tag{2}$$

where ρ is the distance between (x_1,x_2) and (x_1',x_2') and the range of nonlocal actions is controlled by a characteristic length l. The factor $(2\pi l^2)^{-1}$ in (2) normalizes the weight function so that $\int_\Omega \phi(\rho)\mathrm{d}\Omega = 1$. The nonlocal formulation (1) can for sufficiently smooth fields of ξ be rewritten into a gradient formulation around (x_1,x_2) (cf. Lasry and Belytschko, 1988; Mühlhaus and Aifantis, 1991) according to:

$$\xi(x_1',x_2') = \sum_{j=0}^{jn}\sum_{k=0}^{kn}\frac{(x_1'-x_1)^j(x_2'-x_2)^k}{j!k!}\,\frac{\partial^j\partial^k\xi(x_1,x_2)}{\partial x_1^j\partial x_2^k}, \tag{3}$$

where jn and kn denote the order of the series expansion in respective direction (where the 0th order is the functional value itself) and $\partial^j/\partial x_i^j$ denote the jth order of the derivative. Substitution of (3) into (1) yields

$$\bar{\xi}(x_1,x_2) = \xi(x_1,x_2) + a_2\frac{\partial^2\xi(x_1,x_2)}{\partial x_i^2} + a_4\frac{\partial^4\xi(x_1,x_2)}{\partial x_i^2\partial x_j^2} + \cdots \tag{4}$$

Using the weight function ϕ in (2), the constants in (4) is written $a_{2m} = \frac{1}{m!}c^{2m}, m = 1,2,\ldots$ where a length $c^2 = l^2/2$ have been introduced for the sake of convenience. Differentiating (4) twice and substituting back into (4), a truncated implicit formulation is obtained (Peerlings et al., 1996) in form of a modified inhomogeneous Helmholtz equation:

$$\bar{\xi}(x_1,x_2) - c^2\nabla^2\bar{\xi}(x_1,x_2) = \xi(x_1,x_2) \quad \text{in } \Omega, \tag{5}$$

where $\nabla^2 = \partial^2/\partial x_1^2 + \partial^2/\partial x_2^2$ is the Laplacian operator. In (5), derivatives of the fourth order and higher have been neglected. It is assumed that $\bar{\xi}$ admits at least Fréchet derivative. This is an inevitable necessity: if that would not be the case, (5) could not make sense. The interested reader is referred to the abovementioned references

for a thorough description of nonlocal continuum field theory. An advantage of the implicit Eq. (5), compared to the explicit Eq. (4), is that (5) limits a present singularity in the local field while (4) amplifies the singularity.

4. The model

Now, consider a planar isotropic fiber network containing a straight stationary macroscopic crack, Fig. 5. The material is on the macroscopic scale considered linearly elastic and a state of plane stress is assumed to prevail. A Cartesian (x_1,x_2) and a polar coordinate system $(r=[x_1^2+x_2^2]^{1/2}, \theta=\tan^{-1}[x_2/x_1])$ are introduced with their origins coinciding with the crack-tip. The crack occupies the negative part of the x_1-axis, i.e. $x_1<0$ and $x_2=0$, and Ω is the infinite domain containing the crack. Distant from the crack-tip a pure macroscopic mode I opening field acts and the local stress tensor σ_{ij} is given by:

$$\sigma_{ij}=\frac{K_I}{\sqrt{2\pi r}}f_{ij}(\theta) \quad \text{as } r\to\infty, \tag{6}$$

according to Linear Elastic Fracture Mechanics (LEFM) (cf. Williams, 1957) where K_I is the mode I stress intensity factor. The angular functions $f_{ij}(\theta)$, found in every book on fracture mechanics, can be expressed by sums containing two terms according to: $f_{11}(\theta)=\frac{3}{4}\cos\frac{\theta}{2}+\frac{1}{4}\cos\frac{5\theta}{2}, f_{22}(\theta)=\frac{5}{4}\cos\frac{\theta}{2}-\frac{1}{4}\cos\frac{5\theta}{2}$ and $f_{12}(\theta)=-\frac{1}{4}\sin\frac{\theta}{2}+\frac{1}{4}\sin\frac{5\theta}{2}$. The nonlocal stress tensor $\bar\sigma_{ij}$ is calculated using the LEFM stress tensors (6) as source terms in the modified inhomogeneous Helmholtz Eq. (5),

$$\bar\sigma_{ij}-c^2\nabla^2\bar\sigma_{ij}=\sigma_{ij}. \tag{7}$$

Inspired by Aifantis (2011) and Askes and Aifantis (2011), solutions to (7) are obtained by superposition utilizing an ansatz of the form $\bar\sigma_{ij}=K_I(2\pi)^{-1/2}[G_1(r)F_1(\theta)+G_2(r)F_2(\theta)]$, where $G_1(r)$ and $G_2(r)$ are unknown functions and $F_1(\theta)$ and $F_2(\theta)$ are as the first and second terms in $f_{ij}(\theta)$. Thus, $G_1(r)$ is connected to the angular functions having argument $\theta/2$ while $G_2(r)$ is connected to those having angular argument $5\theta/2$. Of special interest in this study is the nonlocal hoop stress $\bar\sigma_{\theta\theta}$ acting in the crack-tip region. Utilizing ordinary transformation rules, $\bar\sigma_{\theta\theta}$ is given by:

$$\bar\sigma_{\theta\theta}=\bar\sigma_{11}\sin^2\theta+\bar\sigma_{22}\cos^2\theta-2\bar\sigma_{12}\sin\theta\cos\theta, \tag{8}$$

where $\bar\sigma_{11},\bar\sigma_{22}$ and $\bar\sigma_{12}$ are the in-plane nonlocal stresses solving (7). Eq. (7) is solved in a previous investigation (Isaksson and Hägglund, 2012) and for the sake of simplicity only the solutions are given here:

$$\begin{aligned}
\bar\sigma_{11}&=\frac{K_I}{\sqrt{2\pi r}}\left[\frac{3}{4}\cos\frac{\theta}{2}[1-e^{-r/c}]+\frac{1}{4}\cos\frac{5\theta}{2}[1-6c^2/r^2+2e^{-r/c}(3c^2/r^2+3c/r+1)]\right]\\
\bar\sigma_{22}&=\frac{K_I}{\sqrt{2\pi r}}\left[\frac{5}{4}\cos\frac{\theta}{2}[1-e^{-r/c}]-\frac{1}{4}\cos\frac{5\theta}{2}[1-6c^2/r^2+2e^{-r/c}(3c^2/r^2+3c/r+1)]\right]\\
\bar\sigma_{12}&=\frac{K_I}{\sqrt{2\pi r}}\left[\frac{-1}{4}\sin\frac{\theta}{2}[1-e^{-r/c}]+\frac{1}{4}\sin\frac{5\theta}{2}[1-6c^2/r^2+2e^{-r/c}(3c^2/r^2+3c/r+1)]\right]
\end{aligned} \tag{9}$$

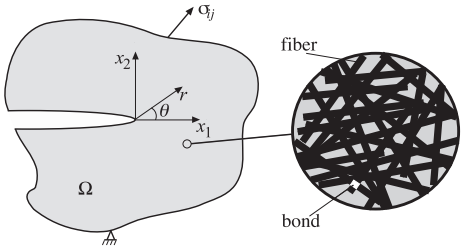

Fig. 5. Geometry and load of the body.

Having in mind that Laplace's operator in polar coordinates is given by $\nabla^2=\partial^2/\partial r^2+r^{-1}\partial/\partial r+r^{-2}\partial^2/\partial\theta^2$, it is easily confirmed that the expressions in (9) satisfies (7). When solving (7), physical requirements of finite stresses at infinity and at the tip were applied to remove singularities, following e.g. Aifantis (2011). The nonlocal elastic strain tensor $\bar\varepsilon_{ij}$ is obtained by the same solution strategy and it turns out that $\bar\varepsilon_{ij}$ is given by Hooke's generalized law $\bar\varepsilon_{ij}=[\bar\sigma_{ij}-\bar\sigma_{kk}\delta_{ij}\nu/(1+\nu)]/E$, where E is Young's modulus, ν is Poisson's ratio and δ_{ij} is Kronecker's delta.

5. Limitations and general and additional assumptions

It is convenient to define a microfracture process as the irreversible process where either a fiber or a fiber–fiber bond breaks, while a plastic process is when there is an irreversible straining of the fibers themselves or frictional effects between fibers. Therefore, supported by experimental observations in Section 2, for fiber materials examined here the governing microfracture mechanism is fiber–fiber bond fracture. Hence, it is in this study assumed that the tensile response of the considered material is, on the macroscopic scale, transversely isotropic and linearly elastic until onset of fracture, i.e. the influence from any plasticity process is assumed negligible. According to the performed and evaluated experiments, these assumptions essentially agree reasonably well with the fracture- and material properties of both the examined paper materials.

Further, since the analysis is restricted to proportionally applied loads, i.e. the square-root singular terms in Eq. (9) are kept proportional, the problem is self-similar (i.e. the solution is of the same form irrespective of the stress intensity factor K_I) and all length variables in the problem scale with the characteristic length c. We have followed e.g. Askes and Aifantis (2011) and assumed vanishing stress- and strain fields at the tip, which is essential for the removal of singularities. This assumption may be questioned. However, the assumption has limited effect and, as will be shown later, the gradients are extremely high when $r\to 0_+$ and the magnitude of stresses and strains changes from high to zero in a short distance, several orders of magnitude lower than the length c. The segment length, i.e. the length between adjacent bonds along a fiber, is therefore considered as a lower bound for the characteristic length (cf. Hägglund and Isaksson, 2006; Isaksson and Hägglund, 2009b). This length is the same order of magnitude as the pore size in the network, i.e. the material's "natural" defect.

6. Numerical results

6.1. Hoop stress

Fig. 6(a) displays contours of normalized nonlocal hoop stress $\bar\sigma_{\theta\theta}$ while in Fig. 6(b) are the nonlocal stress $\bar\sigma_{\theta\theta}$ and local stress $\sigma_{\theta\theta}$ contrasted along the crack plane in-front of the tip. As indicated, at distances $r>2c$ the two hoop stresses are approximately equal. Also, the nonlocal stress field is smoothly distributed around the tip and the singularity is vanished: the stress is finite due to the applied boundary conditions and the position of maximum value is located close to, but not exactly at, the tip. A numerical analysis reveals that the maximum hoop stress $\bar\sigma_{\theta\theta}$ is situated on the crack plane at the distance $r/c=1.095$.

6.2. Hoop strain

Fig. 7(a) shows contours of the nonlocal strain $\bar\varepsilon_{\theta\theta}$ while Fig. 7(b) shows $\bar\varepsilon_{\theta\theta}$ along the crack plane. A Poisson's ratio of $\nu=0.3$ is selected for the sake of convenience. In accordance with the nonlocal stress field, the nonlocal strain is bounded and vanishes at the tip

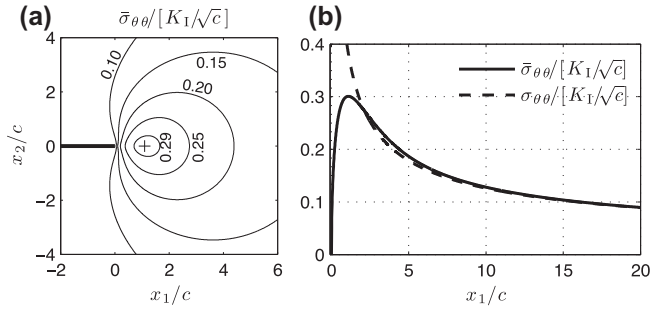

Fig. 6. (a) Contours of nonlocal stress $\bar{\sigma}_{\theta\theta}$, normalized by $K_I/\sqrt{c}$. The position of $\max(\bar{\sigma}_{\theta\theta})$ is marked with + and is located close to, but not exactly at, the tip. (b) Hoop stress in-front of the crack-tip at $\theta = 0$. Notice that $\bar{\sigma}_{\theta\theta} \to 0$ as $r \to 0$ in contrast to its classical counterpart $\sigma_{\theta\theta}$ (LEFM) that has a $r^{-1/2}$-singularity. The maximum $\bar{\sigma}_{\theta\theta}$ is situated on the crack plane at the distance $r/c = 1.095$.

when $r \to 0$, in contrast to the singular classical local strain. The position of maximum hoop strain is located close to, but not exactly at the tip.

6.3. Prediction of crack growth directions

Classical models are not suitable when mechanically analyzing crack growth behavior in network materials and the validity of such models may be heavily questioned for such materials. In the case of symmetric loading and geometry and if the crack size is sufficient to localize fracture, crack growth along a path parallel to the crack plane is to be expected on a macroscopic level. However, on the microscopic level, the crack may grow via infinitesimal kink formations in certain suitable directions, Fig. 8. The maximum tensile stress criterion is based on the concentration of tensile stress at the crack-tip and is the traditional and conventional method to predict mode I failure, cf. Erdogan and Sih (1963). A numerical analysis reveals that the maximum hoop stress $\bar{\sigma}_{\theta\theta}$ is equal to $0.30K_I/\sqrt{c}$ and is situated on the crack plane at the distance $r/c = 1.095$ (Fig. 6). A nonlocal stress contour of the region where relatively high hoop-stresses are acting ($\bar{\sigma}_{\theta\theta}/\max(\bar{\sigma}_{\theta\theta}) = 0.8$) is also drawn in Fig. 8. The almost perfect circular shaped region is positioned immediately in front of the tip and the width Δ of the region is about $3c$. Having in mind that a network have a randomly distributed microstructure, the preferred direction of crack growth is rather diffuse and can be anywhere ahead of the tip in a fairly wide region. Most likely the crack will grow along weak material points in the network's wide diffuse process zone at the tip rather than along a distinct straight path. Microfracture processes will possibly take place simultaneously at several locations and the size of the circle-shaped fracture process zone ahead of the tip is expected to be smaller as the length c decreases.

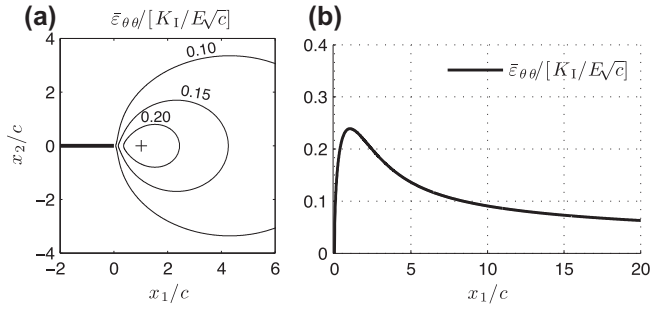

Fig. 7. (a) Contours of the nonlocal strain $\bar{\varepsilon}_{\theta\theta}$, normalized by $K_I/[E\sqrt{c}]$. The position of $\max(\bar{\varepsilon}_{\theta\theta})$ is marked with +. (b) Hoop strain $\bar{\varepsilon}_{\theta\theta}$ in-front of the crack-tip at $\theta = 0$. The position of maximum strain is located close to, but not exactly at, the tip.

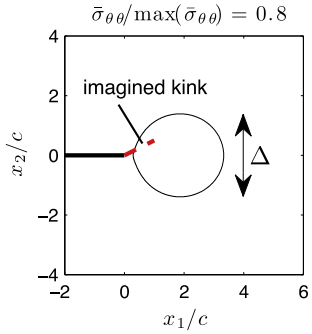

Fig. 8. Contour of nonlocal hoop stress $\bar{\sigma}_{\theta\theta}/\max(\bar{\sigma}_{\theta\theta}) = 0.8$. The almost perfect circular shaped region has a width of approximately $\Delta \approx 3c$. An imagined kink formed at the tip is visualized.

6.4. Comparison to the classical Eringen nonlocal solution

It may be interesting to contrast the present model with Eringen's classical nonlocal theory (cf. Eringen, 2002; Eringen et al., 1977). The finite stress field according to Eringen is obtained utilizing the local LEFM stress tensor σ_{ij} (6) as source term in (7), exactly as here, but the differential equation is solved using a Green's function applied in the infinite domain Ω. Eringen's solution gives an asymptotic hoop stress equal to $6K_I\Gamma\left(\frac{3}{4}\right)^2/[5\pi^{3/2}c^{1/2}]$ at $r = \theta = 0$, in contrast to the assumption made here of a vanishing stress at the tip. In Fig. 9, nonlocal hoop stresses are plotted along the crack plane and as contours around the tip. The maximum hoop stress in Eringen's theory is positioned at $\theta \approx \pm 30°$ and $r/c = 1.055$ and captures a value roughly 1.5 times higher than the maximum hoop stress in the present model.

7. Discussion

An optical non-contact displacement measuring system was used to estimate the strain field in crack-tip regions during fracture tests on a hygiene tissue paper material (Isaksson and Hägglund, 2007). Fig. 10 shows an example of estimated strain measured at a relatively low magnitude of applied load in a specimen containing a straight internal crack. The strain ε_e is measured in a direction transverse to the crack-plane and is plotted versus distance x_1/a in front of a crack-tip located at $x_1 = 0$ ($2a$ is the length of the internal crack). The estimated strain is smooth and continuous even though it fluctuates due to variations in thickness of the material. The experimentally estimated strain is finite at the tip in accordance with the assumptions made (Fig. 7) and implies that the physical

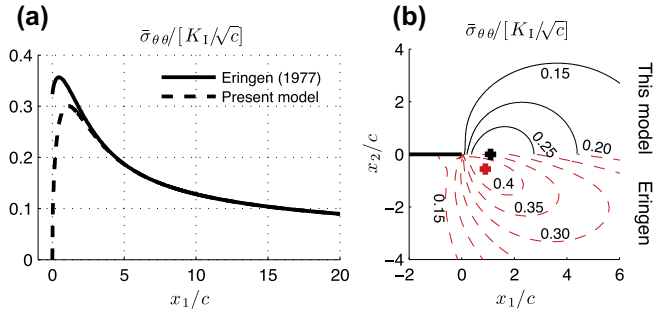

Fig. 9. Comparison of stress $\bar{\sigma}_{\theta\theta}$ in near-tip region estimated by present model and Eringen's theory. (a) Stresses along the crack plane. (b) The stress contours at $x_2 > 0$ are according to the present model while those at $x_2 < 0$ are according to Eringen. The two positions of maximum stress are indicated by + markers. The position of maximum hoop stress is not located on the crack plane in Eringen's theory; an important fact that is overlooked in literature.

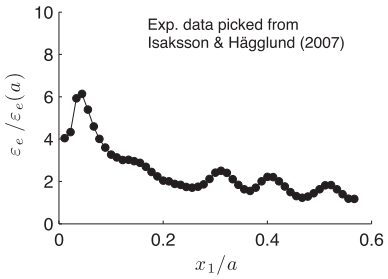

Fig. 10. Experimentally estimated strain ε_e along the crack-plane in a sparse network material. The strain is normalized with its value at $x_1 = a$.

strain field in networks may be described by a nonlocal field theory. This observation is pretty much confirmed with the experimental analysis in Section 2. For both tested network materials, the initial cracks are obviously critical defects. During loading, continued crack growth occurs through diffuse damage processes at the tips and pore-opening phenomena can be observed that are considerably more pronounced in the sparse network. It is also observed that the damaged zone is substantially wider and more diffuse in the low-density material than in the dense, Figs. 3 and 4, well in accordance with the model results, Figs. 6–8. One may also observe that in the sparse paper, crack growth occurs through diffuse kink formation with a deviation from the main crack plane while in the dense paper the crack growth continues from the tip straight ahead. The ability of the model to capture this phenomenon is demonstrated in Fig. 11, where contours of relatively high stress regions ($\bar{\sigma}_{\theta\theta}/\max(\bar{\sigma}_{\theta\theta}) = 0.8$) are drawn utilizing the two different internal lengths $c = 23$ μm and $c = 125$ μm that correspond to the estimated average segment lengths in the materials. The coupling between segment length and internal length is not obvious and surely needs to be explored further. However, it seems fair to assume that the internal length scales linearly to the segment length and therefore, the size of the fracture process zone is expected to relate linearly to the internal length. The region of high stresses is, according to the model, five times larger in the sparse material than in the dense, hence may explain the relatively large diffuse process zone observed in the experiments. When comparing Figs. 3 and 4 it is apparent that the diffuse process zone is substantially larger in the sparse network than in the dense and surely a factor five is of a correct order of magnitude. Thus, in sparse networks, the stress field in the tip region is "smeared" and crack growth can follow many directions due to fewer load carrying structural elements (and more and larger pores) in contrast to dense networks, or classical continua, where crack growth is inclined to the tip and the direction straight ahead along the crack plane. The nonlocal model is capable to qualitatively capture this mechanical behavior as reflected in Fig. 11.

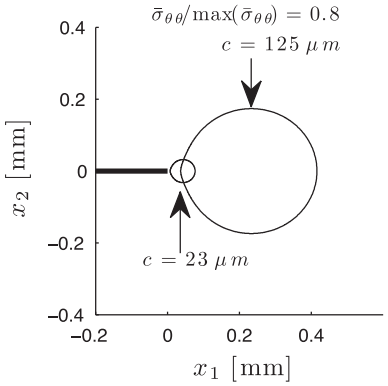

Fig. 11. Contours of $\bar{\sigma}_{\theta\theta}/\max(\bar{\sigma}_{\theta\theta}) = 0.8$ when using internal lengths $c = 125$ μm and $c = 23$ μm, which are equal to the average segment lengths in the sparse and dense network materials used in experiments. The region of high nonlocal hoop stress is around five times larger in the sparse network than in the dense.

These observations are some examples of microstructural features that influence crack growth in fiber-based media and put light on the microstructural evolution mechanisms that accompany continued crack growth. The experimental results unambiguously indicate that there is a microstructural effect that resembles a phenomenon of nonlocal structural action in network materials that most likely explains the observation that sparse network structures, such as tissue papers, are not as sensitive to defects as dense paper materials. With use of Eqs. (8) and (9), a fracture load criterion may be obtained that is expected to handle fractures emerging from defects of different sizes in network materials better than the classical fracture theories manage. It is also possible to estimate the material length c from a series of fracture experiments in which the crack length is varied. It should be underlined that the length c is related to the characteristic segment length in the network wherefore a sparser network is expected to have a higher intrinsic length than a denser. In other words: high-density networks are more "continuum-like" as compared to sparser networks, which is reflected in Figs. 3 and 4. Every fracture experiment performed in this study took several hours to conduct. Due to limitations of available experimental time at ESRF, only one fracture experiment on each material type was possible to conduct in the synchrotron. Even though the limited experiments confirm the theory, additional tests certainly have to be done in order to obtain stronger statistical support. Future work will focus on crack growth phenomena in a set of fiber network media that exhibit larger ranges of densities and lengths of critical defects.

8. Conclusions

The purpose of this study is to contribute to the overall understanding of crack growth mechanisms in fiber networks. This class of material exhibits very specific and complex crack growth behavior that is not well understood and still requires considerable experimental and theoretical achievements. Particularly attention is given to crack growth in opening mode. Both low- and high-density cellulose fiber materials have been used in sophisticated X-ray synchrotron microtomography experiments to illustrate crack growth phenomena. A large influence of the density of the network material on the fracture process is observed. In a dense network, crack growth occurs in a small region at the tip and the continued crack path is inclined to take place along the main crack plane. In contrast, crack deviations through diffuse kinking from the main crack plane is significantly more pronounced in a sparse network, and crack growth can take place more or less simultaneously at several locations in a fairly wide process region at the tip. To capture these fundamental mechanisms, a mechanical model based on a strong nonlocal theory is applied in which an intrinsic length reflects the characteristic length of the microstructure. Nonlocal stress and strain tensor fields are estimated by utilizing analytical solutions on closed form to a modified inhomogeneous Helmholtz equation utilizing LEFM crack-tip fields as source terms. Physical requirements of finite stresses and strains at infinity and at the tip are applied to remove singularities. For materials with large intrinsic lengths, such as sparse networks, it is numerically demonstrated that crack growth possibly occurs in a rather large and wide circle-shaped region in front of the tip. The size and width of this region is approximately linearly decreased as the intrinsic length decreases and ultimately -when the intrinsic length vanishes- crack growth is concentrated to the tip and the direction along the main crack plane, i.e. resembling the mechanical behavior of

a classical brittle continua. The experimental observations are shown to be qualitatively well in accordance with the numerical predictions, which justifies the adopted approach.

Acknowledgements

The Swedish Research Society is acknowledged for the financial support of P. Isaksson. University Joseph Fourier, Grenoble, is gratefully acknowledged for the support of P. Isaksson during a period as visiting professor, spring 2011. The study was partially performed within the framework of the ESRF's long-term project MA127 Heterogeneous Fibrous Materials, of the ANR-09-JCJC-0030-01 project 3D Discrete Analysis of Deformation Micro-Mechanisms in Highly Concentrated Fibre Suspensions.

References

Aifantis, E.C., 2011. On the gradient approach – relation to Eringen's nonlocal theory. Int. J. Eng. Sci. 49, 1367–1377.
Askes, H., Aifantis, E.C., 2011. Gradient elasticity in statics and dynamics: An overview of formulations, length scale identification procedures, finite element implementations and new results. Int. J. Solids Struct. 48, 1962–1990.
Baruchel, J., Buffière, J.-Y., Maire, É., Merle, P., Peix, G. 2000. X-ray tomography in material science. Hermès, Paris.
Batchelor, W.J., He, J., Sampson, W.W., 2006. Inter-fibre contacts in random fibrous materials: experimental verification of theoretical dependence on porosity and fibre width. J. Mater. Sci. 41, 8377–8381.
Bergqvist, H., Guex, L., 1979. Curved crack propagation. Int. J. Fract. 15, 429–441.
Cotterell, B., Rice, J.R., 1980. Slightly curved or kinked cracks. Int. J. Fract. 16, 155–169.
Dzenis, Y., 2004. Spinning continuous fibers for nanotechnology. Science 304, 1917–1919.
Erdogan, F., Sih, G.C., 1963. On the crack extension in plates under plane loading and transverse shear. J. Basic Eng. 85, 519–525.
Eringen, A.C., 2002. Nonlocal Continuum Field Theories. Springer-Verlag, N.Y.
Eringen, A.C., Edelen, D.G.B., 1972. On nonlocal elasticity. Int. J. Eng. Sci. 10, 233–248.
Eringen, A.C., Speziale, C.G., Kim, B.S., 1977. Crack-tip problem in non-local elasticity. J. Mech. Phys. Solids 25, 339–355.
Fleck, N.A., Hutchinson, J.W., 1993. A phenomenological theory for strain gradient effects in plasticity. J. Mech. Phys. Solids 41, 1825–1857.
Fleck, N.A., Hutchinson, J.W., 1997. Strain gradient plasticity. Adv. Appl. Mech. 33, 295–361.
Fleck, N.A., Muller, G.M., Ashb, M.F., Hutchinson, J.W., 1994. Strain gradient plasticity: theory and experiment. Acta Metall. Mater. 42, 475–487.
Gao, H., Huang, Y., Nix, W.D., Hutchinson, J.W., 1999. Mechanism-based strain gradient plasticity – I. Theory J. Mech. Phys. Solids 47, 1239–1263.
Hägglund, R., Isaksson, P., 2006. Analysis of localized failure in low-basis weight paper. Int. J. Solids Struct. 43, 5581–5592.
He, J., Batchelor, W.J., Johnston, R.E., 2004. A microscopic study of fibre–fibre contacts in paper. Appita J. 54, 292–298.
Henriksson, M., Berglund, L.A., Isaksson, P., Lindström, T., Nishino, T., 2008. Cellulose nanopaper structures of high toughness. Biomacromolecules 9, 1579–1585.
Huang, Y., Gao, H., Nix, W.D., Hutchinson, J.W., 2000. Mechanism-based strain gradient plasticity – II. Analysis. J. Mech. Phys. Solids 48, 99–128.
Isaksson, P., Hägglund, R., 2007. Analysis of the strain field in the vicinity of a crack tip in an in-plane isotropic paper material. Int. J. Solids Struct. 44, 656–671.
Isaksson, P., Hägglund, R., 2009a. Structural effects on deformation and fracture of random fiber networks and consequences on continuum models. Int. J. Solids Struct. 46, 2320–2329.
Isaksson, P., Hägglund, R., 2009b. Strain energy distribution in a crack-tip region in random fiber networks. Int. J. Fract. 156, 1–9.
Isaksson, P., Hägglund, R. 2012. Crack-tip fields in gradient enhanced elasticity. Submitted for publications.
Kak, A.C., Slaney, M., 2001. Principles of computerized tomographic imaging. Soc. Indus. Appl. Math.
Kalthoff, J.F., 1973. On the propagation direction of bifurcated cracks. In: Sih, G.C. (Ed.), Dynamic Crack Propagation. Noordhoff International Publishing, Leyden, pp. 49–458.
Kröner, E., 1967. Elasticity theory of materials with long range cohesive forces. Int. J. Solids Struct. 3, 731–742.
Lasry, D., Belytschko, T., 1988. Localization limiters in transient problems. Int. J. Solids Struct. 24, 581–597.
Le Corre, S., Dumont, P., Orgéas, L., Favier, D., 2005. Rheology of highly concentrated planar fiber suspensions. J. Rheol. 49, 1029–1058.
Mentzel, A., Steinmann, P., 2000. On the continuum formulation of higher order gradient plasticity for single and polycrystals. J. Mech. Phys. Solids 48, 1777–1796.
Mühlhaus, H.B., Aifantis, E.C., 1991. A variational principle for gradient plasticity. Int. J. Solids Struct. 28, 845–857.
Peerlings, R.H.J., de Borst, R., Brekelmans, W.A.M., de Vree, J.H.P., 1996. Gradient enhanced damage for quasi-brittle materials. Int. J. Numer. Methods Eng. 39, 3391–3403.
Peerlings, R.H.J., de Borst, R., Brekelmans, W.A.M., de Vree, J.H.P., 2001. A critical comparison of nonlocal and gradient-enhanced softening continua. Int. J. Solids Struct. 38, 7723–7746.
Pijaudier-Cabot, G., Bazant, Z.P., 1987. Nonlocal damage theory. J. Eng. Mech. 113, 1512–1533.
Ridruejo, A., González, C., Llorca, J., 2010. Damage micromechanisms and notch sensitivity of glass-fiber non-wowen felts: an experimental and numerical study. J. Mech. Phys. Solids. 58, 1628–1645.
Ridruejo, A., González, C., Llorca, J., 2011. Micromechanisms of deformation and fracture of polypropylene nonwoven fabrics. Int. J. Solids Struct. 48, 151–162.
Rolland du Roscoat, S., Bloch, J.F., Thibault, X., 2005. Synchrotron radiation microtomography applied to investigation of paper. J. Phys. D Appl. Phys. 38, A78–A84.
Rolland du Roscoat, S., Decain, M., Thibault, X., Geindreau, C., Bloch, J.F., 2007. Estimation of microstructural properties from synchrotron X-ray microtomography and determination of the REV in paper materials. Acta Mater. 55, 2841–2850.
Silling, S.A., 2000. Reformulation of elasticity theory for discontinuities and long-range forces. J. Mech. Phys. Solids 48, 175–209.
Simone, A., Askes, H., Sluys, L.J., 2004. Incorrect initiation and propagation of failure in non-local and gradient-enhanced media. Int. J. Solids Struct. 41, 351–363.
Toll, S., 1993. Note: on the tube model for fiber suspensions. J. Rheol. 37, 123–125.
Viguié, J., Dumont, P.J.J., Mauret, É., Rolland du Roscoat, S., Vacher, P., Desloges, I., Bloch, J.F., 2011. Analysis of the hygroexpansion of a lignocellulosic fibrous material by digital correlation of images obtained by X-ray synchrotron microtomography: application to a folding box board. J. Mater. Sci. 46, 4756–4769.
Williams, M.L., 1957. On the stress distribution at the base of a stationary crack. J. Appl. Mech. 24, 109–114.